Available online at www.sciencedirect.com
ScienceDirect
Trans. Nonferrous Met. Soc. China 34(2024) 1456−1469
Transactions of Nonferrous Metals Society of China
www.tnmsc.cn

Effect of La/Nd ratio on microstructure and tensile properties of AZ91-RE alloys

Peng-xing CUI[1], Mao-liang HU[1,2], Ze-sheng JI[1], Ye WANG[1,2], Yu GUO[3], Hong-yu XU[1,2]

1. School of Materials Science and Chemical Engineering, Harbin University of Science and Technology, Harbin 150080, China;
2. Key Laboratory of Advanced Manufacturing and Intelligent Technology, Ministry of Education, Harbin University of Science and Technology, Harbin 150080, China;
3. School of Intelligent Manufacturing, Huzhou College, Huzhou 313000, China

Received 25 October 2022; accepted 18 September 2023

Abstract: The effect of La/Nd ratio on the microstructure and tensile properties of AZ91-RE alloys was studied. Typical characterization was performed to analyze the volume fraction, mean nearest neighbor distance (NND), and number density of the secondary phases. First-principles calculations were employed to determine the formation enthalpy, mechanical and thermodynamics properties of the secondary phases. The results demonstrate that the alloy with a mass fraction ratio of La to Nd (w_{La}/w_{Nd}) of 3∶2 exhibits the finest average grain size, the smallest mean NND, and the highest total number density of secondary phases. The calculations indicate that the formation of $Al_{11}La_3$ and Al_2Nd is energetically favorable. Furthermore, $Al_{11}La_3$ and Al_2La display significantly superior deformation resistance, shear deformation resistance, solid stiffness and thermal stability compared to other secondary phases. Therefore, increasing the content of $Al_{11}La_3$ and Al_2La phases contributes to improving the mechanical properties of AZ91-RE alloy.

Key words: AZ91 alloy; microstructure; tensile properties; first-principles calculation; electronic structure; thermodynamic properties

1 Introduction

Magnesium alloys hold significant potential as the lightest structural materials in weight-saving systems owing to their low density [1,2]. However, their applications are limited by low strength, especially at an elevated temperature (>120 °C) [3]. The addition of rare earth (RE) elements to Mg−Al alloys has been reported to effectively improve the mechanical properties by forming the Al−RE intermetallic compounds [4,5]. Over the past decades, Mg−Al−RE (AE) alloys (where RE stands for La-rich or Ce-rich mischmetal) have been developed for use in automotive powertrains [6]. The incorporation of RE elements induces the formation of thermally stable $Al_{11}RE_3$ and Al_2RE phases, in which RE elements partially substitute for each other [7]. Light RE elements (La, Ce, Pr, Nd, and Sm) exhibit familiar physical and chemical properties. However, the specific effects of individual RE elements on the microstructures and mechanical properties of AE alloys have been rarely reported until now.

The previous studies by POWELL et al [8] indicated that the formation of $Al_{11}RE_3$ and Al_2RE is sensitive to individual RE elements. They found that the phases with low La/Nd mass ratios (less

Corresponding author: Mao-liang HU, Tel: +86-13936585119, E-mail: humaoliang@hrbust.edu.cn
DOI: 10.1016/S1003-6326(24)66483-6

than 0.7:1) were identified as Al_2RE phases, while the higher ratio was associated with $Al_{11}RE_3$ phases. La preferentially segregates into the $Al_{11}RE_3$ phase, while Nd preferentially segregates into the Al_2RE phase. ZHU et al [9] discussed the microstructure of AE42 alloy, and the EDX results supported the preferential segregation of La into the $Al_{11}RE_3$ phase. Additionally, ZHANG et al [10] calculated the decomposition energy of the $Al_{11}RE_3$ phase using first-principles, and the results showed that $Al_{11}La_3$ has the highest decomposition energy. This indicates that the thermal stability of $Al_{11}RE_3$ is sensitive to individual RE elements, leading to variations in the microstructure and mechanical properties of AE alloys with different La and Nd additions. MENG et al [11] further concluded that the intermetallic components could be altered and controlled by strictly managing the chemical composition of a particular alloy system, opening possibilities for exploring the most excellent mechanical properties of specific alloy systems.

In recent years, the rapid development and application of computational materials science addressed the limitations of experimental methods. Computer simulation methods encompass macroscopic numerical simulation (e.g., finite element method [12]), microstructure simulation (e.g., phase field method and metameric cellular automata [13,14]) and nanomolecular simulation (e.g., first-principle and molecular dynamics [15]). Among them, first-principles calculations based on density functional theory (DFT) offer a convenient and efficient method for understanding and predicting material properties with successful application in the study of metallic materials [16]. WANG et al [17] conducted a study on the electronic structures, elastic properties and thermodynamic properties of the secondary phases in Mg−Al−Ca−Sn alloys. The results showed that Al_2Ca and Mg_2Sn exhibited superior thermal stability and higher properties, thereby enhancing the heat resistance of Mg−Al-based alloys with the addition of Ca and Sn. In view of the ability of first-principles calculations to estimate secondary phase related properties, a study of Mg−Al alloys with the incorporation of RE elements is warranted using this method. Such an investigation provides valuable theoretical and technological guidance for designing Mg−Al−RE alloys and interpreting future experimental results.

The formation of the Al−RE phase in Mg−Al alloys is highly sensitive to rare earth individuals, yet there are limited reports on the effect of rare earth individual differences on the microstructure of Mg−Al alloys. Notably, among the light rare earth elements (La, Ce, Pr, Nd, and Sm), La possesses the largest atomic radius, while Nd has the largest solid solubility in Mg [18]. Due to larger atomic radius of La, this element exhibits a stronger solute drag effect, effectively reducing the grain boundary mobility and inhibiting the precipitation of the discontinuously precipitated $Mg_{17}Al_{12}$ phase. On the other hand, the larger solid solubility of Nd reduces the diffusion rate of aluminum atoms in the magnesium matrix. Additionally, La preferentially segregates into the $Al_{11}RE_3$ phase, while Nd partitions into the Al_2RE phase. The morphology and number of secondary phases ($Al_{11}RE_3$, Al_2RE, and $Mg_{17}Al_{12}$) vary with the contents of La and Nd. Although the shape, quantity, and distribution of the secondary phases significantly affect the tensile properties of the alloys, it remains unclear how different mass fraction ratios of La to Nd (w_{La}/w_{Nd}) affect the microstructures and tensile properties of Mg−Al alloys, as well as the changes in the mechanical and thermomechanical properties of the secondary phases with the La and Nd contents. Therefore, further investigation of the effect of the w_{La}/w_{Nd} ratio on the microstructure and tensile properties is necessary.

To address this research gap, the present study aims to modify the microstructure and mechanical properties of AZ91-RE alloy by meticulously controlling the w_{La}/w_{Nd} ratio. Furthermore, the first-principles method was employed based on the DFT to study the properties of the secondary phases in AZ91-RE alloy and analyze the effect of RE on the second phase from the electronic structure perspective.

2 Experimental

2.1 Materials preparation

In this study, AZ91-RE alloys with different w_{La}/w_{Nd} ratios were prepared. Commercial AZ91D ingot, Mg−15wt.%La and Mg−20wt.%Nd master alloys were used to achieve the target compositions. In the casting process, the alloys were melted in a resistance furnace with a graphite crucible and protected by a gas mixture of 99 vol.% CO_2 and

1 vol.% SF_6. The melt was stirred for 3 min and held for 20 min to ensure homogeneous melting. The slag flux was eliminated using a refining agent and the melt was poured into the preheated Y-type steel mold (as shown in Fig. 1(a)). The chemical composition of AZ91-RE alloys was determined using inductively coupled plasma−atomic emission spectroscopy (ICP−AES), and the results are listed in Table 1.

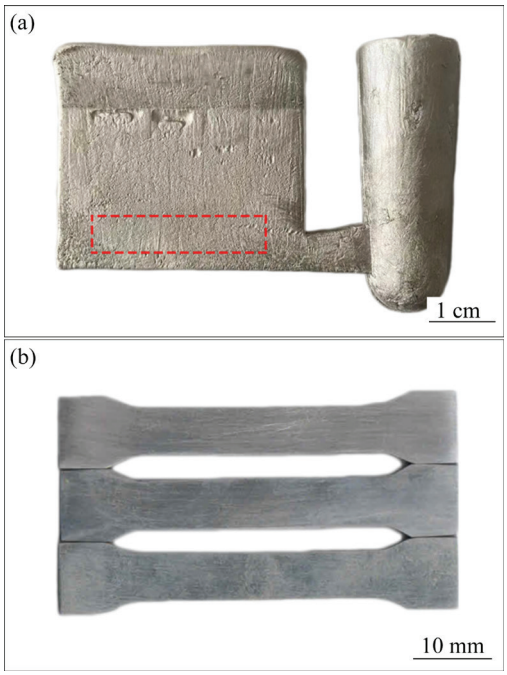

Fig. 1 Photograph of specimen (a) and tensile samples (b)

Table 1 Chemical compositions of as-cast G1−G6 alloys

Alloy code	w_{La}/w_{Nd}	Content/wt.%				
		La	Nd	Al	Zn	Mg
G1	0:0	0.00	0.00	8.69	0.74	Bal.
G2	1:3	0.52	1.48	8.47	0.77	Bal.
G3	2:3	0.77	1.21	8.64	0.72	Bal.
G4	1:1	0.98	1.02	8.52	0.73	Bal.
G5	3:2	1.20	0.77	8.60	0.74	Bal.
G6	3:1	1.47	0.54	8.59	0.77	Bal.

2.2 Characterization techniques

The tensile samples (as shown in Fig. 1(b)) were obtained through spark machining at the marked position in Fig. 1(a). Tensile tests were conducted using an electronic universal testing machine (AG-X Plus by Shimadzu) with an initial strain rate of 0.001 s^{-1}. In order to ensure statistical significance, three samples were tested under identical conditions to obtain the average value. The microstructure was characterized using an ultra-depth-of-field digital microscope (DM, DSX1000 by Olympus), scanning electron microscopy (SEM, Apreo C, operating at 20 kV) equipped with energy-dispersive X-ray spectrometry (EDS, OXFORD INCA X-ACT) and transmission electron microscopy (TEM, JEM−2100 operating at 200 keV). For optical microscopy (OM) analysis, the samples (8 mm × 8 mm × 15 mm) were lightly polished and etched using the reagent containing 6 g picric acid, 5 mL glacial acetic acid, 100 mL alcohol and 10 mL distilled water. The average grain size was determined using Image-Pro Plus 6.0 software. The samples (8 mm × 8 mm × 15 mm) for SEM analysis were carefully mechanically polished and etched using the reagent of 4 mL HNO_3 and 95 mL ethyl alcohol. Thin foil samples (d1.5 mm × 40 μm) for TEM analysis were prepared by ion-milling using a PIPS II system (Gatan 695).

2.3 Computational details

First-principles calculations were accomplished with the "Cambridge Sequential Total Energy Package (CASTEP)" code, which is based on the DFT. This approach solves the Kohn−Sham equations by expanding the valence electron density and wave function through the plane-wave pseudo-potentials method [19,20]. The exchange-correlation function in the electron−electron interaction was treated using the generalized gradient approximation (GGA) with the Perdew−Burke−Ernzerhof (PBE) function [21]. An effective Broyden−Fletcher−Goldfarb−Shanno (BFGS) method was applied for the geometry optimization of the crystal structure [22]. The cut-off energy was tested using different values and 450 eV was selected for all calculations. The phonon calculations were conducted using the finite displacement method with the phonons properties package [23,24].

3 Results

3.1 Microstructure observation

Figure 2 presents metallographic micrographs of the as-cast G1−G6 alloys. The images of all alloys were taken from the same position of the specimens. The AZ91 alloy (G1) exhibits a dendrite grain structure, while AZ91-RE alloys (G2−G6) display an equiaxed grain structure. With varying

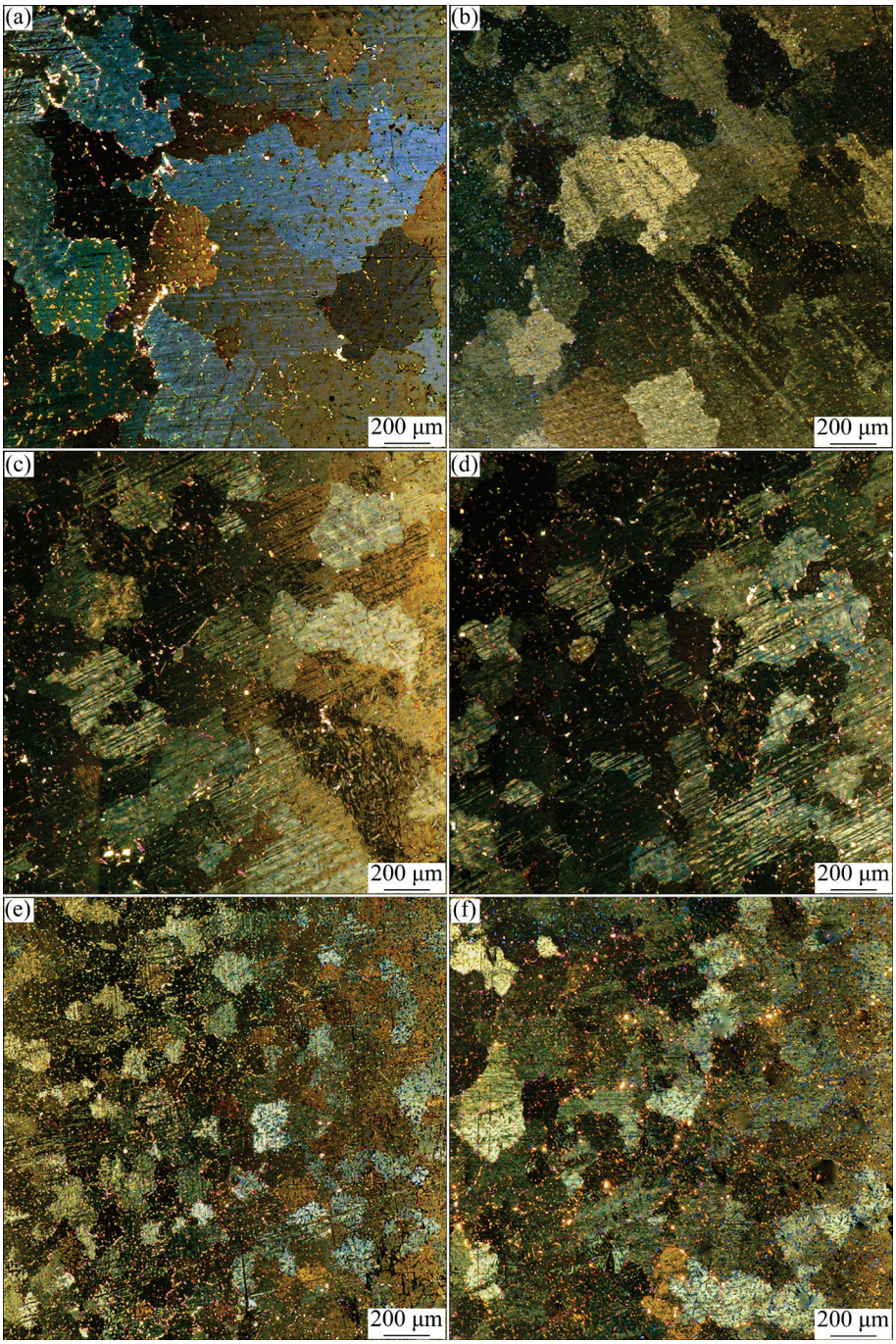

Fig. 2 Metallographic micrographs of as-cast G1−G6 alloys: (a) G1; (b) G2; (c) G3; (d) G4; (e) G5; (f) G6

w_{La}/w_{Nd} ratios in the AZ91-RE alloys, a noticeable transition from coarse dendritic crystals to fine fully equiaxed crystals is observed due to the growth restricting effect [25]. The average grain sizes of G1−G6 alloys are measured to be (376±27), (208±22), (177±21), (154±19), (115±16) and (144±17) μm, respectively. Notably, as the w_{La}/w_{Nd} ratio increases, the average grain size initially decreases significantly and then experiences a slight increase. Among all the alloys, the alloy with w_{La}/w_{Nd} of 3∶2 exhibits the smallest grain size.

Figure 3 displays the SEM images of the as-cast G1−G6 alloys. The microstructure of AZ91 alloy (G1) consists of α-Mg grains and coarse β-$Mg_{17}Al_{12}$ phase. As RE elements are added into AZ91 alloy, Al−RE phases form in the AZ91-RE alloy. According to the SEM images in Figs. 3(b−f), the main secondary phases of AZ91-RE alloys are characterized by a dark-gray bulk phase, a bright-white acicular phase, and a granular phase.

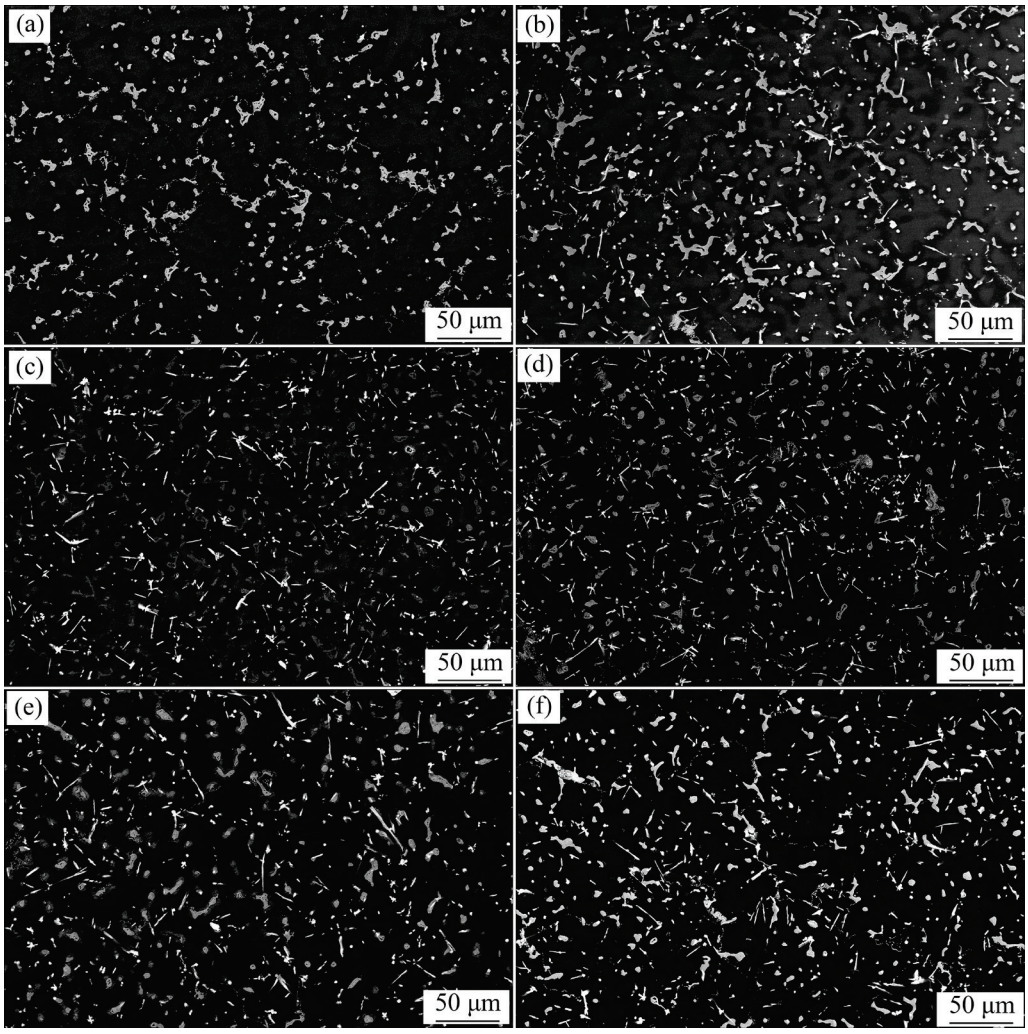

Fig. 3 SEM images of as-cast G1−G6 alloys: (a) G1; (b) G2; (c) G3; (d) G4; (e) G5; (f) G6

Figure 4 presents the SEM image of G4 alloy and Table 2 lists the corresponding EDS results. The EDS analysis at Point *A* confirms that the dark-gray phase is composed of Mg and Al. Bright-filed TEM (BF-TEM) observation (Fig. 5(a)) further verifies that this phase corresponds to the β-$Mg_{17}Al_{12}$ phase, formed through the divorced eutectic reaction [26]. Moreover, the bright-white acicular phase (labeled as *B* in Fig. 4) and granular phase (labeled as *C* in Fig. 4) are identified to be composed of Al and RE (La and Nd). The indexing of the selected area electron diffraction (SAED) patterns (Figs. 5(b) and (c)) indicates that the acicular phase corresponds to $Al_{11}RE_3$ with an orthorhombic crystal structure (a=0.44 nm, b=1.01 nm and c=1.31 nm), while the granular phase corresponds to Al_2RE with a diamond crystal structure (a=0.80 nm) [11,27]. Furthermore, the EDS results demonstrate that the intensity of the La peak is markedly higher in the acicular phase and

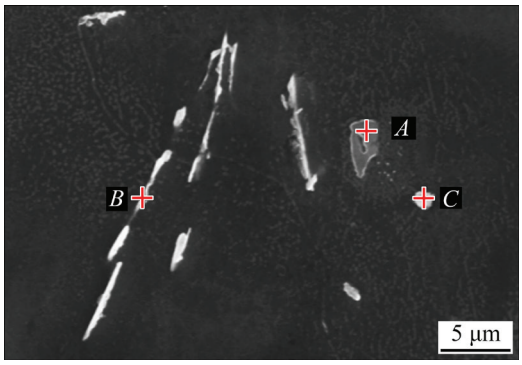

Fig. 4 SEM image of G4 alloy

the intensity of the Nd peak is significantly higher in the granular phase. These results indicate that La segregates preferentially into the acicular phase while Nd segregates preferentially into the granular phase.

Table 3 presents the quantitative analysis results of the secondary phases in G1−G6 alloys. With the addition of RE, a significant decrease occurs in the

Table 2 EDS results of Points *A*, *B*, and *C*

Element	Content/wt.%			Content/at.%		
	Point *A*	Point *B*	Point *C*	Point *A*	Point *B*	Point *C*
Mg	69.66	56.71	40.96	71.41	68.99	53.19
Al	33.19	24.31	29.97	35.18	26.65	35.07
Zn	1.48	0.14	0.27	0.65	0.74	0.13
La	0	12.19	2.69	0	2.98	0.61
Nd	0	6.52	11.27	0.01	1.74	2.47

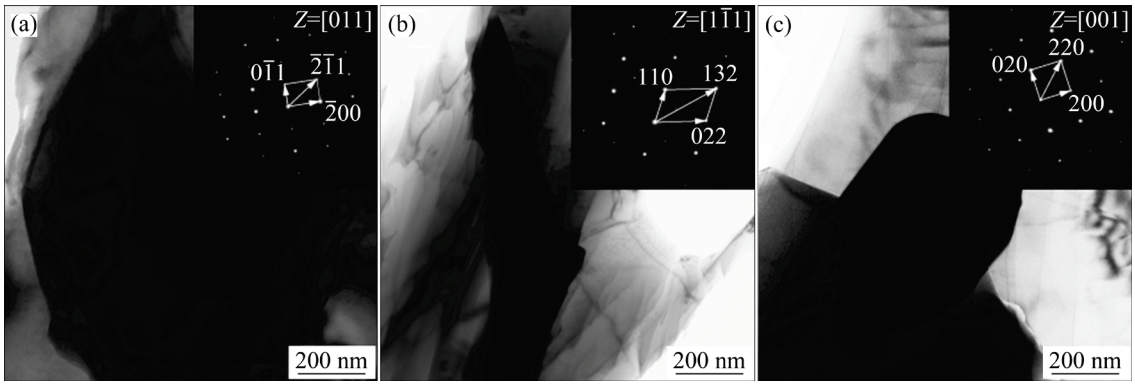

Fig. 5 BF-TEM images and corresponding SAED patterns of secondary phases in AZ91-RE alloys: (a) β-$Mg_{17}Al_{12}$; (b) $Al_{11}RE_3$; (c) Al_2RE

Table 3 Quantitative analysis results of secondary phases

Alloy code	Phase	Volume fraction/%	Mean NND/μm
G1	β-$Mg_{17}Al_{12}$	23.45	35
	$Al_{11}RE_3$	−	
	Al_2RE	−	
G2	β-$Mg_{17}Al_{12}$	7.95	29
	$Al_{11}RE_3$	2.78	
	Al_2RE	2.01	
G3	β-$Mg_{17}Al_{12}$	6.96	26
	$Al_{11}RE_3$	2.91	
	Al_2RE	1.74	
G4	β-$Mg_{17}Al_{12}$	5.43	25
	$Al_{11}RE_3$	3.21	
	Al_2RE	1.63	
G5	β-$Mg_{17}Al_{12}$	3.65	22
	$Al_{11}RE_3$	3.39	
	Al_2RE	1.14	
G6	β-$Mg_{17}Al_{12}$	3.96	23
	$Al_{11}RE_3$	3.65	
	Al_2RE	1.02	

volume fraction of the β-$Mg_{17}Al_{12}$ phase. Moreover, the volume fractions of bulk β-$Mg_{17}Al_{12}$ and granular Al_2RE phases decrease with increasing w_{La}/w_{Nd} ratio, while the volume fraction of acicular $Al_{11}RE_3$ phase increases. Notably, as the w_{La}/w_{Nd} ratio increases from 1∶3 to 3∶2, the total amount of intermetallic compound particles increases, and the mean nearest neighbor distance (NND) decreases. Among the alloys, G5 exhibits the highest number of particles and the smallest mean NND. Figure 6 shows the number density of $Al_{11}RE_3$ and Al_2RE phases measured per square millimeter area (mm^{-2}) in the SEM images of the AZ91-RE alloys. As the w_{La}/w_{Nd} ratio increases, the number density of $Al_{11}RE_3$ phase increases, and the number density of Al_2RE phase decreases, while that of β-$Mg_{17}Al_{12}$ phase first decreases and then exhibits a slight increase.

3.2 Mechanical properties

Figure 7 depicts the tensile true stress−strain curves of the as-cast G1−G6 alloys at room temperature (RT, 25 °C) and elevated temperature (ET, 150 °C). The ultimate tensile strength (UTS), tensile yield strength (TYS) and elongation (EL) of

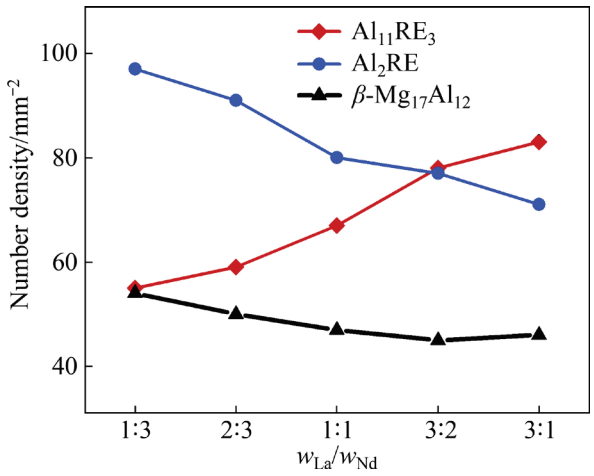

Fig. 6 Number density of $Al_{11}RE_3$, Al_2RE, and β-$Mg_{17}Al_{12}$ phases

the tested alloys are summarized in Table 4. With the addition of RE, the UTS and TYS of AZ91 alloy (at both RT and ET) are significantly improved. Furthermore, the EL of AZ91-RE alloys is notably greater than that of AZ91 alloy, which is attributed to the grain size refinement achieved through RE addition. Notably, the G5 alloy exhibits the highest UTS and TYS at RT, surpassing those of the AZ91 alloy by 19 and 13 MPa, respectively. The AZ91-RE alloys also demonstrate excellent tensile properties at ET, indicating that the addition of RE mitigates the detrimental effect of softening caused by β-$Mg_{17}Al_{12}$ in AZ91 alloy at high temperatures (>120 °C). The UTS, TYS and EL of the AZ91-RE alloy at ET follow the same trend as those at RT, i.e., they increase with increasing w_{La}/w_{Nd}, reaching the maximum at w_{La}/w_{Nd} of 3:2.

4 Discussion

4.1 Enthalpies of formation

Figure 8 displays the crystal structures of the investigated intermetallic compounds. All the crystal structures of phases were optimized within the framework of density functional theory (DFT).

The enthalpy of formation per atom at 0 K for A_xB_y (ΔH_f) was calculated by the following equation:

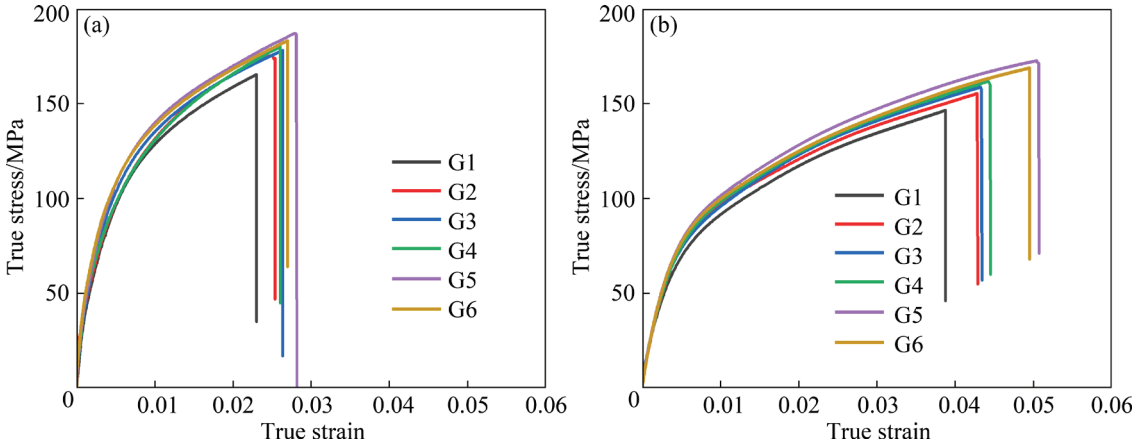

Fig. 7 Tensile true stress−strain curves of as-cast G1−G6 alloys at RT (a) and ET (b)

Table 4 Ultimate tensile strength (UTS), tensile yield strength (TYS) and elongation (EL) of as-cast G1−G6 alloys at RT and ET

Alloy	Tensile property at RT (25 °C)			Tensile property at ET (150 °C)		
	UTS/MPa	TYS/MPa	EL/%	UTS/MPa	TYS/MPa	EL/%
G1	165±5.1	96±1.4	2.2±0.3	141±3.8	71±1.5	3.9±0.2
G2	172±3.4	100±3.3	2.5±0.2	154±3.3	79±2.3	4.2±0.3
G3	176±4.8	96±2.5	2.6±0.2	157±2.8	82±2.2	4.3±0.2
G4	179±4.4	101±3.8	2.6±0.2	164±3.2	87±3.1	4.4±0.3
G5	184±4.7	109±3.6	2.8±0.3	169±2.7	92±2.6	5.1±0.4
G6	183±5.2	103±3.5	2.7±0.4	165±2.8	89±2.8	4.9±0.3

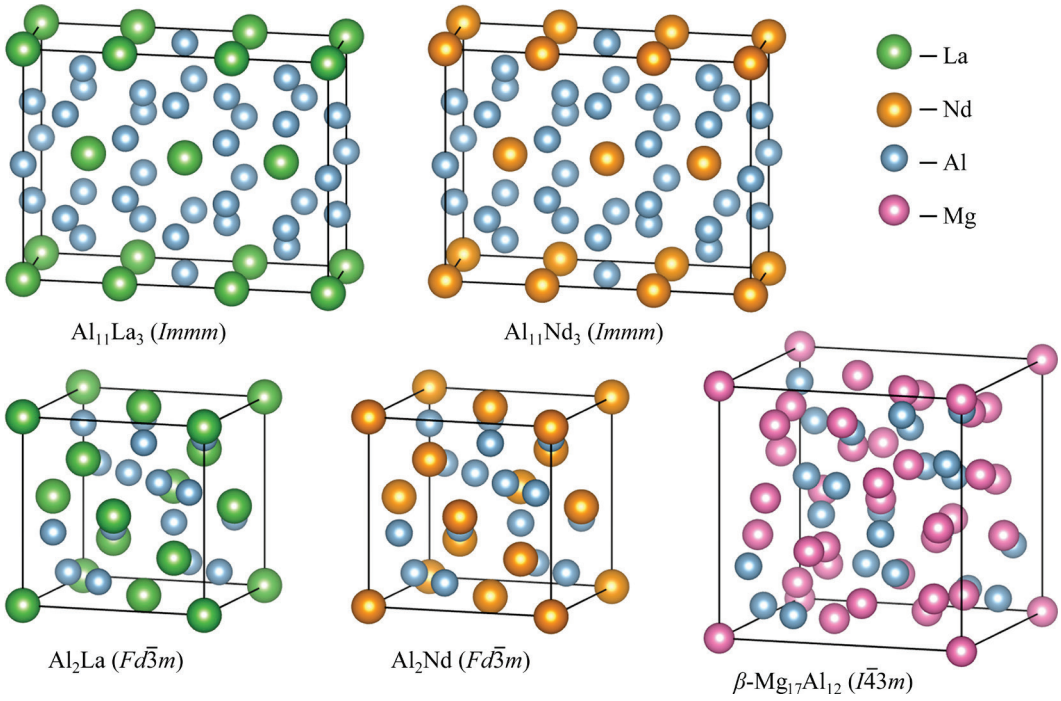

Fig. 8 Crystal structures of studied intermetallic compounds

$$\Delta H_f = \frac{1}{x+y}[E(A_xB_y) - xE(A) - yE(B)] \quad (1)$$

where $E(A_xB_y)$ is the total energy of the A_xB_y intermetallic compound, x and y are the numbers of A and B atoms in the unit cell of A_xB_y phase, respectively, E(A) and E(B) are the energies per atom of A and B crystals in the free state. Figure 9 shows the computed formation enthalpy of the investigated intermetallic compounds at the ground state of the system. Furthermore, the enthalpies of formation reported in Refs. [28−30] are compared with the results obtained in this study, demonstrating excellent quantitative agreement. According to the fitted curves, the convex hull of the Al−La curve skews toward Al side, while the convex hull of Al−Nd curve skews toward Nd side [31]. The enthalpy of Al_2Nd is lower than that of Al_2La, indicating that the formation of Al_2Nd is energetically favorable. While the enthalpy of $Al_{11}La_3$ is lower than that of $Al_{11}Nd_3$, indicating that the formation of $Al_{11}La_3$ is energetically favorable. These findings corroborate the observations made in Refs. [8,9] regarding the preferential segregation of Nd into the granular Al_2RE phase and La into the acicular $Al_{11}RE_3$ phase.

For AZ91-RE alloys with lower w_{La}/w_{Nd}, a higher content of the granular Al_2RE phase is observed from the microstructure since Nd is chemically high and Al_2Nd is energetically favorable (e.g., G2 alloy shown in Fig. 3(b)). For AZ91-RE alloys with higher w_{La}/w_{Nd}, the high content of La accelerates the peritectic reaction of Eq. (2) [32,33] and La preferentially segregates into the acicular $Al_{11}RE_3$ phase. Hence, the content of the acicular $Al_{11}RE_3$ phase increases with the increasing w_{La}/w_{Nd} and higher $Al_{11}RE_3$ content is obtained in the alloy with higher w_{La}/w_{Nd} (e.g., G5 alloy shown in Fig. 3(e)).

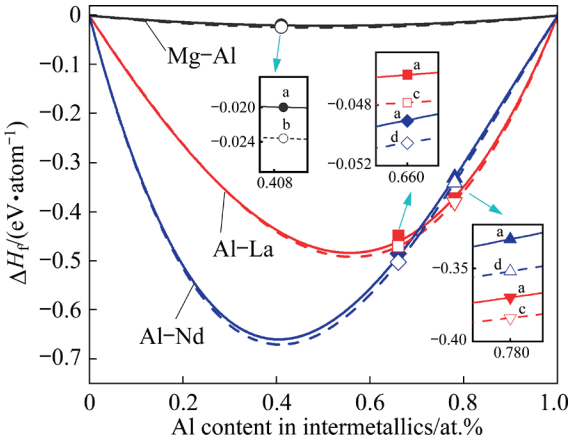

Fig. 9 Calculated formation energy ΔH_f along with experimental and theoretical results for intermetallic compounds from Refs. [28−30] ([a] Cal. in this work, [b] [28], [c] [29], and [d] [30])

$$Al_2RE + L \rightarrow Al_{11}RE_3 \quad (2)$$

4.2 Differential charge density

According to the binary phase diagrams of Mg−La and Mg−Nd, the maximum solid solubilities of La and Nd in Mg are 0.14 at.% and 0.63 at.%, respectively. Due to their low solid solubilities in Mg, supercell models of Mg_{150} and $Mg_{149}RE_1$ were established to study their solid solubility. Figure 10 shows the crystal structure and electron density difference between Mg_{150} and $Mg_{149}RE_1$ supercells. The formation enthalpies of $Mg_{149}La_1$ and $Mg_{149}Nd_1$ are −0.006 and −0.052 eV/atom, respectively, indicating that the solid solution in Mg is rather limited for both and slightly higher solubility for Nd in Mg [34]. Figures 10(d) and (e) depict the electron density contour plots of $Mg_{149}La_1$ and $Mg_{149}Nd_1$ on the $(\bar{2}00)$ plane, respectively. According to Fig. 10(d), charge accumulation is observed between Mg and La atoms and the overlapping electron cloud exhibits strong polarity, indicating that the Mg—La bond is stronger than the corresponding Mg—Mg bond and that La has a strengthening effect. However, when La atom is replaced with Nd atom, the interatomic charge density changes significantly and the charge around RE atoms is redistributed. Since the ability to form a stable structure is primarily related to the Mg−RE interaction, the variations in charge transfer and bond strength between the Mg and RE atoms affect the overall stability of the system. To quantify these variations, population analysis was performed on individual supercells.

Population analysis evaluates the ability of atoms to gain or lose electrons by analyzing the atomic charge numbers, while overlapping population values assess the extent of electron cloud overlap in bonded atoms. Tables 5 and 6 present the average charge populations and overlapping populations for each system, respectively. Due to a large number of atoms in the system, the population numbers and overlapping population values were averaged. La and Nd are electron-gaining

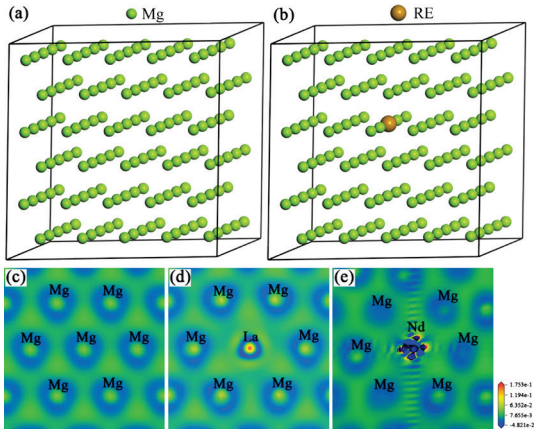

Fig. 10 Crystal structures of Mg_{150} (a) and $Mg_{149}RE_1$ (b) supercells, and electron density difference of Mg_{150} (c), $Mg_{149}La_1$ (d) and $Mg_{149}Nd_1$ (e)

Table 5 Charge populations of each system

System	Atom	s	p	d	Total	Charge
Mg_{150}	Mg	0.89	7.11	0	8.01	0
$Mg_{149}La_1$	Mg	0.88	7.11	0	8.01	0
	La	2.29	6.18	2.56	11.03	0.98
$Mg_{149}Nd_1$	Mg	1.16	6.84	0	8.01	0
	Nd	2.76	6.13	0.57	13.31	0.69

in their respective systems, while Mg is electron-losing. In the $Mg_{149}La_1$ system, the number of electrons gained by La atoms significantly increases, indicating that electrons transfer to La atoms. The overlapping population value of Mg−La suggests the formation of stronger covalent bonds with neighboring Mg atoms. Conversely, in the $Mg_{149}Nd_1$ system, the Nd atom gains electrons, and its covalent bond with the neighboring Mg atom is weaker compared to the covalent bond formed by La and Mg.

The analysis indicates that the electron cloud density of La in the system is higher than that of Nd, and La has a larger atomic radius than Nd. La exhibits a stronger solute dragging effect, leading to

Table 6 Overlapping populations of each system

Bond	Mg_{150}		$Mg_{149}La_1$		$Mg_{149}Nd_1$	
	Population	Length/nm	Population	Length/nm	Population	Length/nm
Mg—Mg	0.0019	0.6879	0.0075	0.2759	0.0063	0.2861
Mg—La			0.0875	0.7067		
Mg—Nd					0.0128	0.7418

decreased grain boundary mobility and suppression of discontinuous precipitates formation. Thus, with an increase in w_{La}/w_{Nd}, the content of La atoms increases, further strengthening the diffusion inhibition and solute dragging effect, which hinders the precipitation process of β-$Mg_{17}Al_{12}$ phase [35]. The volume fraction of β-$Mg_{17}Al_{12}$ phase decreases with the increase of w_{La}/w_{Nd}. On the other hand, the solid solution of Nd in Mg matrix is greater than that of La. When w_{La}/w_{Nd} is greater than 3∶2, the inhibition of Al atom diffusion by RE is weakened due to the decrease of Nd, leading to coarsening of the β-$Mg_{17}Al_{12}$ grains in the alloy.

4.3 Mechanical properties

The properties of β-$Mg_{17}Al_{12}$, Al_2La, $Al_{11}La_3$, Al_2Nd and $Al_{11}Nd_3$ compounds were investigated by calculating elastic constants C_{ij} based on the stress−strain method of Hooke's law. The β-$Mg_{17}Al_{12}$, Al_2La and Al_2Nd compounds with cubic crystal structure have three independent elastic constants, which are C_{11}, C_{12}, and C_{44}, respectively. The restrictions of Born stability criterion for cubic structure are shown as follows [36]:

$$\begin{cases} C_{11} > 0 \\ C_{44} > 0 \\ C_{11} + 2C_{12} > 0 \end{cases} \tag{3}$$

The $Al_{11}La_3$ and $Al_{11}Nd_3$ compounds with orthorhombic crystal structure have nine independent elastic constants (C_{11}, C_{12}, C_{13}, C_{22}, C_{23}, C_{33}, C_{44}, C_{55}, and C_{66}). For orthorhombic crystals, the criteria to be considered mechanically stable are shown as follows:

$$\begin{cases} C_{ii} > 0 \ \ (i = 1,\ 2,\ 3,\ 4,\ 5,\ 6) \\ C_{11} + C_{22} - 2C_{12} > 0 \\ C_{22} + C_{33} - 2C_{23} > 0 \\ C_{11} + C_{33} - 2C_{13} > 0 \\ C_{11} + C_{22} + C_{33} + 2C_{12} + 2C_{13} + 2C_{23} > 0 \end{cases} \tag{4}$$

The calculated elastic constants for β-$Mg_{17}Al_{12}$, Al_2La, $Al_{11}La_3$, Al_2Nd, $Al_{11}Nd_3$ are listed in Table 7. The bulk modulus (B), shear modulus (G), Young's modulus (E) and Poisson ratio (ν) of these phases are respectively calculated by Eqs. (5)−(8) and the calculation results are tabulated in Table 8.

$$B = 1/3(C_{11} + 2C_{12}) \tag{5}$$

$$G = 1/5(3C_{44} + C_{11} - C_{12}) \tag{6}$$

$$E = \frac{9BG}{3B + G} \tag{7}$$

$$\nu = \frac{3B - 2G}{6B + 2G} \tag{8}$$

The deformation resistance, shear deformation resistance as well as solid stiffness of $Al_{11}La_3$ and Al_2La are substantially superior to those of the other phases, as evidenced by their higher B, G and E values. Consequently, it is reasonable to expect that the yield strength of AZ91-RE alloys increases with increasing w_{La}/w_{Nd} due to the higher content of the energetically favorable Al−La phase. As for the Pugh modulus ratio (B/G), according to the empirical formula of Pugh, materials with B/G ratios greater than 1.75 exhibit ductile behavior under applied stress [37]. Furthermore, materials with higher ν values tend to display better plasticity of the material structural behavior. Although the β-$Mg_{17}Al_{12}$ phase exhibits the best ductility among these phases, its B/G value increases by only 0.27 over the critical value. AZ91 alloy exhibits brittleness due to massive aggregation of eutectic reaction product β-$Mg_{17}Al_{12}$. The addition of RE to AZ91 significantly reduces the content of β-$Mg_{17}Al_{12}$, resulting in an increase in the ductility of the alloy. The B/G and ν values of $Al_{11}La_3$ and Al_2La are close to those of β-$Mg_{17}Al_{12}$, and they maintain comparable ductility and plasticity to β-$Mg_{17}Al_{12}$. Thus, the elongation of AZ91-RE alloys increases with the increasing w_{La}/w_{Nd} due to the increased chemical composition of La and the increased content of Al−La phase.

Table 7 Calculated elastic constants of β-$Mg_{17}Al_{12}$, Al_2La, Al_2Nd, $Al_{11}La_3$, and $Al_{11}Nd_3$ (GPa)

Phase	C_{11}	C_{12}	C_{13}	C_{22}	C_{23}	C_{33}	C_{44}	C_{55}	C_{66}
β-$Mg_{17}Al_{12}$	89.19	28.57				20.69			
Al_2La	136.68	31.24					40.78		
Al_2Nd	120.93	13.29					24.52		
$Al_{11}La_3$	112.42	46.01	47.25	114.50	47.36	109.77	48.03	50.24	58.66
$Al_{11}Nd_3$	−143.82	33.43	61.43	98.07	−7.55	113.03	28.56	78.24	14.78

Table 8 Calculated bulk modulus (B), shear modulus (G), Yong's modulus (E), Pugh modulus ratio (B/G) and Poisson ratio (v) of intermetallic compounds at zero pressure

Alloy	B/GPa	G/GPa	E/GPa	B/G	v
$Mg_{17}Al_{12}$	48.78	24.12	62.12	2.02	0.28
$Al_{11}La_3$	68.65	43.22	107.19	1.58	0.23
$Al_{11}Nd_3$	37.83	31.53	74.04	1.19	0.17
Al_2La	66.38	45.20	110.52	1.46	0.22
Al_2Nd	49.17	33.79	82.48	1.45	0.22

4.4 Thermodynamic properties

Phonon calculations were performed to evaluate the enthalpy (H), entropy (S), Gibbs free energy (G_1) and specific heat capacity (C_v) of these phases as a function of temperature according to Eqs. (9)−(12), respectively [38]:

$$H(T)=E(A_xB_y)+E_{zp}+\int\frac{\hbar\omega}{\exp(\hbar\omega/(k_BT))}F(\omega)\,d(\omega) \quad (9)$$

$$S(T)=k_B\left\{\int\frac{\hbar\omega/(k_BT)}{\exp(\hbar\omega/(k_BT))-1}F(\omega)\,d(\omega)-\int F(\omega)\ln[1-\exp(-\hbar\omega/(k_BT))]\,d(\omega)\right\} \quad (10)$$

$$G_1(T)=E(A_xB_y)+E_{zp}+k_BT\int\ln[1-\exp(-\hbar\omega/(k_BT))]F(\omega)\,d(\omega) \quad (11)$$

$$C_v(T)=k_B\int\frac{(\hbar\omega/(k_BT))^2\exp(\hbar\omega/(k_BT))}{[\exp(\hbar\omega/(k_BT))-1]^2}F(\omega)\,d(\omega) \quad (12)$$

where E_{zp} is the zero point energy, $\hbar$ is the Planck constant, k_B is the Boltzmann constant, $F(\omega)$ is the phonon density of states, and T is the temperature.

Figure 11(a) shows the enthalpies of β-$Mg_{17}Al_{12}$, Al_2La, Al_2Nd, $Al_{11}La_3$, and $Al_{11}Nd_3$ phases. Before the temperature increases to 187 K, the decreasing order of enthalpy magnitudes is $Al_{11}Nd_3$ > $Al_{11}La_3$ > β-$Mg_{17}Al_{12}$ > Al_2La > Al_2Nd. In the range of 187−688 K, the decreasing order of enthalpy magnitudes changes to $Al_{11}Nd_3$ > β-$Mg_{17}Al_{12}$ > $Al_{11}La_3$ > Al_2La > Al_2Nd. When the temperature

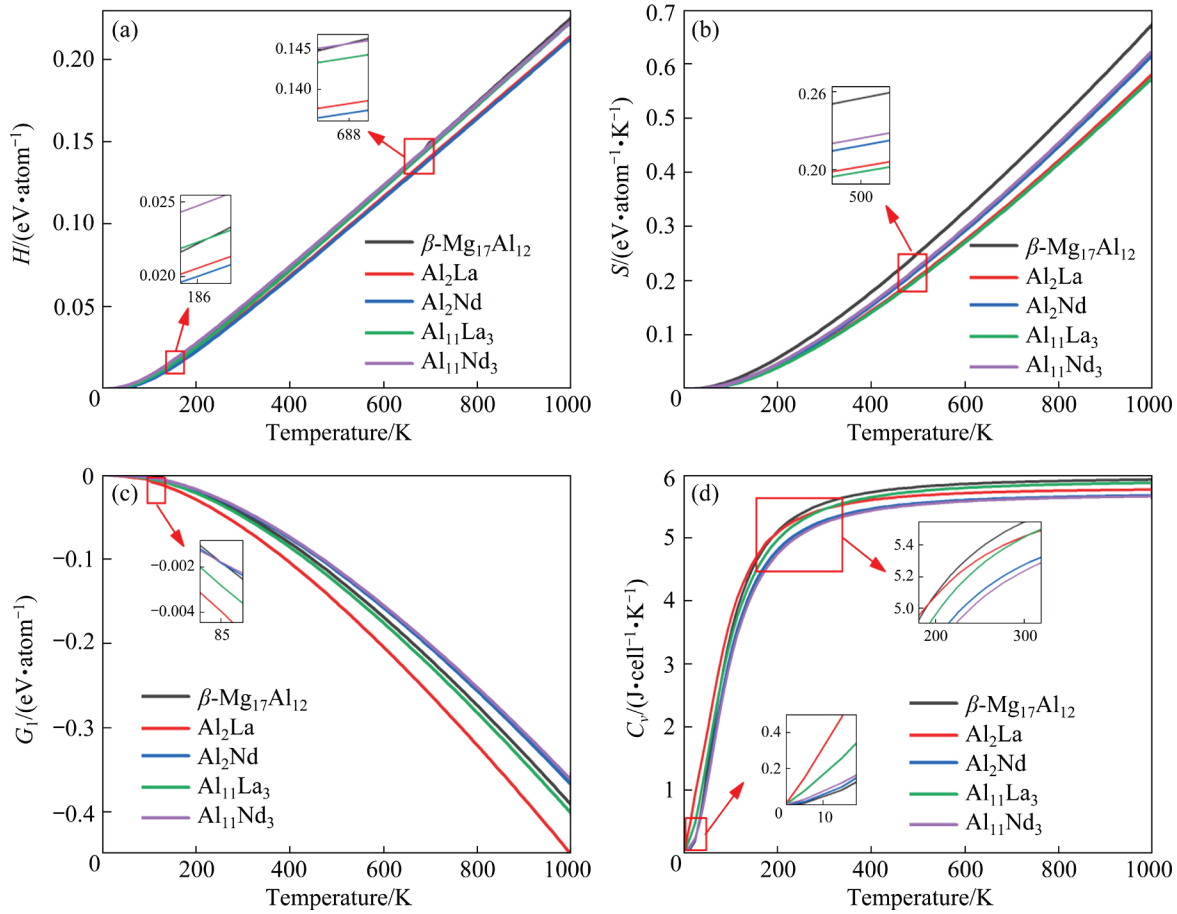

Fig. 11 Thermodynamic properties of vibrational enthalpy (H) (a), entropy (S) (b), Gibbs free energy (G_1) (c) and specific heat capacity (C_v) (d) for intermetallic compounds

exceeds 688 K, the enthalpy decreasing order is $Mg_{17}Al_{12}$ > $Al_{11}Nd_3$ > $Al_{11}La_3$ > Al_2La > Al_2Nd. Figure 11(b) shows the calculated entropies for these phases. All five phases are thermodynamic stable at their respective equilibrium volumes, as no negative values appear. The entropy of β-$Mg_{17}Al_{12}$ phase is significantly larger than that of the other phases and increases rapidly with the increase of temperature. Their entropies follow the decreasing sequence of β-$Mg_{17}Al_{12}$ > $Al_{11}Nd_3$ > Al_2Nd > Al_2La > $Al_{11}La_3$, which indicates that the stiffness of the interatomic bonds for the five intermetallic compounds follows the following decreasing order $Al_{11}La_3$ > Al_2La > Al_2Nd > $Al_{11}Nd_3$ > β-$Mg_{17}Al_{12}$. Al−RE phases may exhibit greater bulk modulus and smaller average atomic volume due to their stiffer interatomic bonds [39], and $Al_{11}La_3$ has the greatest bulk modulus, consistent with the elastic constant analysis above. Figure 11(c) shows the calculated Gibbs free energies of these phases. When the temperature is below 85 K, their Gibbs free energies follow a decreasing sequence as β-$Mg_{17}Al_{12}$ > Al_2Nd > $Al_{11}Nd_3$ > Al_2La > $Al_{11}La_3$. As the temperature increases, the trend of Grbbs free energy increase is Al_2La < $Al_{11}La_3$ < β-$Mg_{17}Al_{12}$ < Al_2Nd < $Al_{11}Nd_3$. That is, the thermal stability of compounds follows the decreasing sequence of Al_2La > $Al_{11}La_3$ > β-$Mg_{17}Al_{12}$ > Al_2Nd > $Al_{11}Nd_3$ at higher temperatures [17]. Figure 11(d) shows the variation of the specific heat capacities C_v versus temperature. The specific heat capacity of β-$Mg_{17}Al_{12}$ is the smallest among these intermetallic compounds in the temperature range below 100 K. As the temperature increases, the specific heat capacity of β-$Mg_{17}Al_{12}$ increases rapidly and becomes the largest when the temperature reaches 190 K. For temperature above 300 K, the specific heat capacities of these intermetallic compounds follow a decreasing sequence as β-$Mg_{17}Al_{12}$ > $Al_{11}La_3$ > Al_2La > Al_2Nd > $Al_{11}Nd_3$, and they converge to their Dulong−Petit limits at high temperatures, which is common for all solids [40,41].

Overall, the Al−Nd phase exhibits lower enthalpy and is more likely to form during the crystallization process. The Al−La phase has lower entropy and Gibbs free energy, leading to superior mechanical properties and thermal stability. Although the β-$Mg_{17}Al_{12}$ phase possesses higher thermal stability than the Al−Nd phase, its mechanical properties are lower, especially at high temperatures. Therefore, it is suggested to reduce the content of β-$Mg_{17}Al_{12}$ in the alloy. The theoretical analysis aligns well with the experimental results, indicating that the Al−La phase, particularly the dominant $Al_{11}La_3$ phase with excellent mechanical properties, could effectively strengthen the AZ91-RE alloy. Notably, the alloy with a w_{La}/w_{Nd} ratio of 3∶2 exhibits the lowest content of eutectic β-$Mg_{17}Al_{12}$ phase and the highest content of Al−La phase, resulting in optimal mechanical properties both at RT and ET. In conclusion, the addition of RE elements, particularly optimizing the w_{La}/w_{Nd} ratio, enhances the mechanical properties and thermal stability of AZ91-RE alloys, with the Al−La phase playing a crucial role in providing significant strengthening. The alloy with a w_{La}/w_{Nd} ratio of 3∶2 demonstrates the most favorable combination of microstructure and mechanical properties, making it a promising candidate for practical engineering applications.

5 Conclusions

(1) The microstructure observation indicates that the alloy with w_{La}/w_{Nd} of 3∶2 has the smallest average grain size, the highest number density of particles and the smallest mean NND. According to the tensile test results, the alloy with w_{La}/w_{Nd} of 3∶2 exhibits the optimal UTS and TYS both at RT and ET.

(2) The formation enthalpies of various compounds, namely β-$Mg_{17}Al_{12}$, Al_2La, $Al_{11}La_3$, Al_2Nd and $Al_{11}Nd_3$, have been calculated using first-principles calculations. The enthalpy of Al_2Nd is lower than that of Al_2La, indicating that the formation of Al_2Nd is energetically favorable. While the enthalpy of $Al_{11}La_3$ is lower than that of $Al_{11}Nd_3$.

(3) The elastic properties of β-$Mg_{17}Al_{12}$, Al_2La, $Al_{11}La_3$, Al_2Nd and $Al_{11}Nd_3$ were calculated. The deformation resistance, shear deformation resistance as well as solid stiffness of $Al_{11}La_3$ and Al_2La are substantially superior to those of the other phases. In addition, $Al_{11}La_3$ and Al_2La maintain a ductility and plasticity comparable to those of β-$Mg_{17}Al_{12}$.

(4) Based on the thermodynamic calculations, the Al−Nd phase has lower enthalpy and the Al−La phase has lower entropy and Gibbs free energy. As

the temperature increases, the Al−La phase is more thermally stable and has higher mechanical properties. The alloys with higher Al−La phase content and lower β-$Mg_{17}Al_{12}$ phase content exhibit higher mechanical properties.

CRediT authorship contribution statement

Peng-xing CUI: Original draft, Investigation, Methodology, Data curation; **Mao-liang HU:** Resources, Supervision, Writing − Review & editing; **Ze-sheng JI:** Funding acquisition, Supervision; **Ye WANG:** Visualization, Investigation; **Yu GUO:** Software, Validation; **Hong-yu XU:** Visualization, Writing − Review & editing.

Declaration of competing interest

The authors declare that they have no known competing financial interests or personal relationships that could have appeared to influence the work reported in this paper.

Acknowledgments

This study was financially supported by the National Key Research and Development Program of China (No. 2019YFB2006500), the National Natural Science Foundation of China (Nos. 51574100, 51704087), and the Natural Science Foundation of Heilongjiang Province, China (No. LH2020E083).

References

[1] LIU W, ZHAO Y H, ZHANG Y T, SHUAI C, CHEN L W, HUANG Z Q, HOU H. Deformation-induced dynamic precipitation of 14H-LPSO structure and its effect on dynamic recrystallization in hot-extruded Mg−Y−Zn alloys [J]. International Journal of Plasticity, 2023, 164: 103573.

[2] LIU S S, YANG B P, HUANG G S, CHEN X H, TANG A T, JIANG B, ZHENG K H, PAN F S. Effect of dual-heterogeneous microstructures on mechanical properties of AZ91 extruded sheet [J]. Transactions of Nonferrous Metals Society of China, 2023, 33(4): 1086−1097.

[3] XU J, GUAN B, XIN Y C, WEI X D, HUANG G J, LIU C L, LIU Q. A weak texture dependence of Hall−Petch relation in a rare-earth containing magnesium alloy [J]. Journal of Materials Science & Technology, 2022, 99: 251−259.

[4] KARA İ H. Wear behavior of hot rolled AZ31B and AZ31B−Nd−La Mg alloys tested at different angles to rolling direction [J]. Journal of Materials Engineering and Performance, 2022, 31: 4925−4933.

[5] FU L, GUO C R, ZHANG Z Q, JIA Z, LU L, LE Q C. Study on the microstructure and mechanical properties of as-extruded AZ magnesium alloys by micro-adding La rare-earth element [J]. Shock and Vibration, 2022, 2022: 1453344.

[6] LUO A A. Recent magnesium alloy development for elevated temperature applications [J]. International Materials Reviews, 2004, 49(1): 13−30.

[7] XU C, NAKATA T, FAN G H, YAMANAKA K, TANG G Z, GENG L, KAMADO S. Effect of partially substituting Ca with mischmetal on the microstructure and mechanical properties of extruded Mg−Al−Ca−Mn-based alloys [J]. Acta Metallurgica Sinica (English Letters), 2019, 32(2): 205−217.

[8] POWELL B R, REZHETS V, BALOGH M P, WALDO R A. Microstructure and creep behavior in AE42 magnesium die-casting alloy [J]. JOM, 2002, 54(8): 34−38.

[9] ZHU S M, GIBSON M A, NIE J F, EASTON M A, ABBOTT T B. Microstructural analysis of the creep resistance of die-cast Mg−4Al−2RE alloy [J]. Scripta Materialia, 2008, 58(6): 477−480.

[10] ZHANG J H, LIU K, FANG D Q, QIU X, TANG D X, MENG J. Microstructure, tensile properties, and creep behavior of high-pressure die-cast Mg−4Al−4RE−0.4Mn (RE=La, Ce) alloys [J]. Journal of Materials Science, 2009, 44(8): 2046−2054.

[11] MENG F Z, LV S H, YANG Q, QIN P F, ZHANG J H, GUAN K, HUANG Y D, HORT N, LI B S, LIU X J, MENG J. Developing a die casting magnesium alloy with excellent mechanical performance by controlling intermetallic phase [J]. Journal of Alloys and Compounds, 2019, 795: 436−445.

[12] BIAN Z Y, ZHU A L, XIAO Y K, LI Y G, MA N H, BIAN H B, WANG M L, CHEN Z, WANG H W. Coupling analysis on controlling mechanisms for creep of Al−Fe−Ni alloy [J]. Transactions of Nonferrous Metals Society of China, 2023, 33(5): 1331−1344.

[13] ZHAO Y H. Understanding and design of metallic alloys guided by phase-field simulations [J]. NPJ Computational Materials, 2023, 9(1): 94.

[14] CHEN L Q, ZHAO Y H. From classical thermodynamics to phase-field method [J]. Progress in Materials Science, 2022, 124: 100868.

[15] YU W, CHONG X Y, GAN M D, WEI Y, ZHANG A M, HU C Y, FENG J. Effect of alloying elements on thermoelastic properties of Pt-based alloys [J]. Transactions of Nonferrous Metals Society of China, 2023, 33(6): 1851−1861.

[16] XIN T Z, ZHAO Y H, MAHJOUB R, JIANG J X, YADAV A, NOMOTO K, NIU R M, TANG S, JI F, QUADIR Z, MISKOVIC D, DANIELS J, XU W Q, LIAO X Z, CHEN L Q, HAGIHARA K, LI X Y, RINGER S, FERRY M. Ultrahigh specific strength in a magnesium alloy strengthened by spinodal decomposition [J]. Science Advances, 2021, 7(23): eabf3039.

[17] WANG F, SUN S J, YU B, ZHANG F, MAO P L, LIU Z. First principles investigation of binary intermetallics in Mg−Al−Ca−Sn alloy: Stability, electronic structures, elastic properties and thermodynamic properties [J]. Transactions of Nonferrous Metals Society of China, 2016, 26(1): 203−212.

[18] CUI P X, HU M L, JI Z S, XU H Y, ZHANG X, ZHANG T R. Effect of La/Nd ratio on precipitation kinetics and tensile properties of squeeze-cast Mg−Al−Zn−La−Nd alloys [J]. Materials Today Communications, 2022, 33: 104710.

[19] CLARK S J, SEGALL M D, PICKARD C J, HASNIP P J, PROBERT M I J, REFSON K, PAYNE M C. First principles methods using CASTEP [J]. Zeitschrift für Kristallographie−Crystalline Materials, 2005, 220(5/6): 567−570.

[20] WANG S, LI D, XIONG J. Prediction of elastic properties of face-centered cubic high-entropy alloys by machine learning [J]. Transactions of Nonferrous Metals Society of China, 2023, 33(2): 518−530.

[21] XIAO Y, LAN X Y, LU Q, DU Y, LI K. In-situ evidence for rotation of Si particles with respect to grains in tensile-deformed Al−Si alloys [J]. Transactions of Nonferrous Metals Society of China, 2023, 33(6):

1655−1664.
[22] WANG J J, LU Z J, ZHANG K X, YING G B, LI B S, CHEN J Q, SONG D, JIANG J H, MA A B. DFT study on termination stabilities of $Mg_{17}Al_{12}$ (110) surface [J]. Transactions of Nonferrous Metals Society of China, 2023, 33(3): 755−764.
[23] MONTANARI B, HARRISON N M. Lattice dynamics of TiO_2 rutile: Influence of gradient corrections in density functional calculations [J]. Chemical Physics Letters, 2002, 364(5): 528−534.
[24] ZHOU J Q, HU B, LI B F, DU Y, WANG J. Experimental investigation and thermodynamic modeling of Cu−Nb−Si system [J]. Transactions of Nonferrous Metals Society of China, 2023, 33(3): 824−838.
[25] LIAO H B, MO L L, LI C B, ZHAN M Y, DU J. Grain refinement of Mg−Al binary alloys inoculated by in-situ oxidation [J]. Transactions of Nonferrous Metals Society of China, 2022, 32(10): 3212−3221.
[26] FU Y T, LI Y X, HU A, HU H, NIE X Y. Microstructure, tensile properties and fracture behavior of squeeze-cast Mg alloy AZ91 with thick cross section [J]. Journal of Materials Engineering and Performance, 2020, 29(6): 4130−4141.
[27] SU M L, ZHANG J H, FENG Y, BAI Y J, WANG W, ZHANG Z W, JIANG F C. Al−Nd intermetallic phase stability and its effects on mechanical properties and corrosion resistance of HPDC Mg−4Al−4Nd−0.2Mn alloy [J]. Journal of Alloys and Compounds, 2017, 691: 634−643.
[28] ZHENG B, ZHAO L, HU X B, DONG S J, LI H. First-principles studies of $Mg_{17}Al_{12}$, Mg_2Al_3, Mg_2Sn, $MgZn_2$, Mg_2Ni and Al_3Ni phases [J]. Physica B (Condensed Matter), 2019, 560: 255−260.
[29] SUN F E, ZHANG G W, REN X Y, WANG M J, XU H, FU Y Z, TANG Y Q, LI D Y. First-principles studies on phase stability, anisotropic elastic and electronic properties of Al−La binary system intermetallic compounds [J]. Materials Today Communications, 2020, 24: 101101.
[30] LV S H, LI Y W, MENG F Z, DUAN Q, YANG Q, LIU X J, MENG J. Thermodynamic stability of $Al_{11}RE_3$ intermetallic compounds from first-principles calculations [J]. Computational Materials Science, 2017, 131: 28−34.
[31] LIU C C, LU S, FU Y Y, ZHANG H Q. Flammability and the oxidation kinetics of the magnesium alloys AZ31, WE43, and ZE10 [J]. Corrosion Science, 2015, 100: 177−185.
[32] CACCIAMANI G, FERRO R. Thermodynamic modeling of some aluminium−rare earth binary systems: Al−La, Al−Ce and Al−Nd [J]. Calphad, 2001, 25(4): 583−597.
[33] ZOU H H, ZENG X Q, ZHAI C Q, DING W J. Effects of Nd on the microstructure of ZA52 alloy [J]. Materials Science and Engineering A, 2005, 392(1): 229−234.
[34] SU J, GUO F, GAO X B, FENG H Q. Study on solid-solution interaction and existing forms of alloying elements in Mg−Al−Zn−Gd alloy [J]. Journal of Alloys and Compounds, 2021, 854: 156209.
[35] ROBSON J D. Effect of rare-earth additions on the texture of wrought magnesium alloys: The role of grain boundary segregation [J]. Metallurgical and Materials Transactions A, 2014, 45(8): 3205−3212.
[36] GUO Y, WANG Y, CHEN H J, XU H Y, HU M L, JI Z S. Evaluation of stabilities and thermophysical properties of Si−Sr intermetallics based on first-principles analysis [J]. Results in Physics, 2020, 18: 103207.
[37] BIDAI K, AMERI M, AMERI I. A first-principles study on structural, thermodynamics and elastic properties of $XNBa_3$ (X=As, Sb) under pressure and temperature effect [J]. Optik, 2016, 127(5): 3150−3157.
[38] HU W C, LIU Y, LI D J, ZENG X Q, XU C S. Mechanical and thermodynamic properties of Al_3Sc and Al_3Li precipitates in Al−Li−Sc alloys from first-principles calculations [J]. Physica B (Condensed Matter), 2013, 427: 85−90.
[39] GHOSH G, ASTA M. First-principles calculation of structural energetics of Al−TM (TM=Ti, Zr, Hf) intermetallics [J]. Acta Materialia, 2005, 53(11): 3225−3252.
[40] CHEN H L, LIN L, MAO P L, LIU Z. Phase stability, electronic, elastic and thermodynamic properties of Al−RE intermetallics in Mg−Al−RE alloy: A first principles study [J]. Journal of Magnesium and Alloys, 2015, 3(3): 197−202.
[41] PANG M J, ZHAN Y Z, WANG H Z, JIANG W P, DU Y. Structural, electronic, elastic and thermodynamic properties of $AlSi_2RE$ (RE=La, Ce, Pr and Nd) from first-principle calculations [J]. Computational Materials Science, 2011, 50(12): 3303−3310.

La/Nd 比对 AZ91-RE 合金显微组织和拉伸性能的影响

崔鹏星[1]，胡茂良[1,2]，吉泽升[1]，王 晔[1,2]，郭 宇[3]，许红雨[1,2]

1. 哈尔滨理工大学 材料科学与化学工程学院，哈尔滨 150080；
2. 哈尔滨理工大学 先进制造智能化技术教育部重点实验室，哈尔滨 150080；
3. 湖州学院 智能制造学院，湖州 313000

摘 要：研究 La/Nd 比对 AZ91-RE 合金显微组织和拉伸性能的影响。采用经典表征方法分析第二相的体积分数、平均最近邻距离(NND)和数量密度。利用第一性原理计算确定第二相的形成焓、力学性能和热力学性质。结果表明，La 与 Nd 的质量分数比(w_{La}/w_{Nd})为 3/2 的合金具有最小的平均晶粒尺寸、最小的平均最近邻距离和最高的第二相数量密度。计算结果表明，$Al_{11}La_3$ 和 Al_2Nd 的形成在能量上有利。此外，$Al_{11}La_3$ 和 Al_2La 在抗变形能力、抗剪切变形能力、固体刚度和热稳定性方面都明显优于其他第二相。因此，提高 $Al_{11}La_3$ 和 Al_2La 相的含量有利于改善 AZ91-RE 合金的力学性能。

关键词：AZ91 合金；显微组织；拉伸性能；第一性原理计算；电子结构；热力学性质

(Edited by Wei-ping CHEN)